# nature computational science

**Article** 

https://doi.org/10.1038/s43588-025-00898-3

# Efficient algorithms for the surface density of states in topological photonic and acoustic systems

Received: 4 January 2025

Accepted: 30 September 2025

Published online: 14 November 2025

Check for updates

Yi-Xin Sha <sup>1,2</sup> ⋈, Ming-Yao Xia <sup>3</sup>, Ling Lu <sup>4</sup> & Yi Yang <sup>1,2</sup> ⋈

Topological photonics and acoustics have attracted wide research interest for their ability to manipulate light and sound at surfaces. The supercell technique is the conventional standard approach used to calculate these boundary effects, but, as the supercell grows in size, this method requires increasingly large computational resources. Additionally, it falls short in differentiating the surface states at opposite boundaries and, due to finite-size effects, from bulk states. Here, to overcome these limitations, we provide two complementary efficient methods for obtaining the ideal topological surface states of semi-infinite systems of diverse surface configurations. The first is the cyclic reduction method, which is based on iteratively inverting the Hamiltonian for a single unit cell, and the other is the transfer matrix method, which relies on eigenanalysis of a transfer matrix for a pair of unit cells. Numerical benchmarks, including gyromagnetic photonic crystals, valley photonic crystals, spin-Hall acoustic crystals and quadrupole photonic crystals, jointly show that both methods can effectively sort out the boundary modes via the surface density of states, at reduced computational cost and increased speed. Our computational schemes enable direct comparisons with near-field scanning measurements, thereby expediting the exploration of topological artificial materials and the design of topological devices.

Topological photonic and acoustic crystals have emerged as versatile platforms for exploring topological physics and have thus attracted considerable interest in recent years¹-8. One of their remarkable features is that their surface states are robust against defects and disorder, which brings the potential to realize useful devices such as waveguides, antennas, splitters, isolators and lasers⁰-15. To study surface effects, calculating the band structure of a supercell (a finite-sized slab) has always been the method of choice, but it has several drawbacks. One problem is that it is hard to distinguish the surface states on both sides of the slab unless the eigenfunctions are calculated and examined¹6. Another issue is that the slab thickness should be large enough to avoid spurious coupling between the surface states at the two boundaries,

leading to substantial consumption of computational resources  $^{17}$ . Most importantly, the surface bands are mixed with the bulk bands, and the results cannot be directly compared with a surface state spectrum measured in near-field scanning experiments  $^{18}$ .

The key to solving these problems is the surface Green's function for a semi-infinite system. From this one can derive surface properties such as the surface density state spectrum at a single well-defined boundary. Mathematically, the surface Green's function can be evaluated as the inverse of a Hamiltonian with a block-Toeplitz tridiagonal structure<sup>19</sup>. General direct solvers such as lower–upper and Cholesky factorization scale poorly with increasing system size<sup>20</sup>. Fortunately, certain algorithms<sup>21</sup> can substantially enhance the computational

<sup>1</sup>Department of Physics and HK Institute of Quantum Science and Technology, The University of Hong Kong, Hong Kong, China. <sup>2</sup>State Key Laboratory of Optical Quantum Materials, The University of Hong Kong, Hong Kong, China. <sup>3</sup>State Key Laboratory of Photonics and Communications, School of Electronics, Peking University, Beijing, China. <sup>4</sup>Institute of Physics, Chinese Academy of Sciences/Beijing National Laboratory for Condensed Matter Physics, Beijing, China. ⊠e-mail: yxsha@hku.hk; yiyg@hku.hk

efficiency if the Toeplitz property is fully considered. These primarily fall into two categories. One category comprises iterative techniques, such as the cyclic reduction method (CRM)<sup>22</sup>, and the other semi-analytical techniques such as the transfer matrix method (TMM)<sup>23</sup>. Historically, Golub and Hockney first proposed the CRM for the rapid calculation of the inverse of a scalar-cyclic operator when solving Poisson equations<sup>24–26</sup>. It was then extended to deal with block-cyclic<sup>27</sup> and semi-infinite<sup>22</sup> systems. Simultaneously, Lee and Joannopoulos put forward a TMM for efficiently inverting the Hamiltonian for Schrödinger equations in semi-infinite systems<sup>23</sup>, which is similar to the core idea of the subsequently developed Mobius transformation method<sup>28</sup>. Recently, Colbrook and colleagues proposed another method to rigorously compute the surface spectra of semi-infinite systems by using rectangular truncations that preserve all couplings between the truncated finite region and the remaining infinite bulk<sup>29,30</sup>.

These mathematical advances have been successfully transferred to studies in electronic systems. For example, CRMs in plane-wave and tight-binding bases have been used to calculate the electronic transmission of carbon nanotubes and semiconductors <sup>17,31</sup>. Meanwhile, TMMs based on tight-binding models have been used to investigate the decay of surface states in graphenes <sup>32,33</sup> and to image the surface bands of superconductors and topological insulators <sup>16,34</sup>. So far, these methods have been widely used to analyze and design the surface properties of electronic materials <sup>35–37</sup> and have been developed as a powerful tool for exploring novel topological phenomena <sup>38</sup>.

In photonic and acoustic systems, however, the mathematical advances have not been fully exploited. Although a CRM in a finite-element basis has been proposed to calculate the surface states of photonic and acoustic topological semimetals<sup>39,40</sup>, the formulation is limited to the case of a bare semi-infinite structure. Meanwhile, a TMM based on a plane-wave basis has been presented to simulate the wave propagation in more complex cases such as sandwiched photonic crystals<sup>41,42</sup>, but with such non-localized basis functions it is hard to describe optical fields in metallic materials and sound waves in rigid bodies.

In this Article, to address the above limitations, we implement the CRM and TMM using finite-element discretization in photonic and acoustic systems and provide computational paradigms across a variety of scenarios, including a bare semi-infinite crystal, a semi-infinite crystal with a surface defect, two semi-infinite crystals interfaced with each other, and two semi-infinite crystals with an interface defect. We demonstrate the utility of our approach by calculating the surface state spectra of gyromagnetic photonic crystals, valley photonic crystals, spin-Hall acoustic crystals and the corner state spectra of quadrupole photonic crystals, and compare the differences in the computational efficiency and accuracy of the two methods.

# Results

# Green's functions and local density of states

Green's functions in photonic (equation (1a)) and acoustic (equation (1b)) systems can be defined as the solutions of the wave equations for a point source:

$$[\underbrace{\nabla \times \mu^{-1}(\mathbf{r}) \cdot \nabla \times -\omega^{2} \varepsilon(\mathbf{r})}_{Z(\mathbf{r}, \omega)}] G(\mathbf{r}, \mathbf{r}'; \omega) = I\delta(\mathbf{r} - \mathbf{r}')$$
(1a)

$$\underbrace{\left[\nabla \cdot \rho^{-1}(\mathbf{r})\nabla + \omega^{2}K^{-1}(\mathbf{r})\right]}_{Z(\mathbf{r};\omega)}G(\mathbf{r},\mathbf{r}';\omega) = \delta(\mathbf{r} - \mathbf{r}')$$
 (1b)

where  $\mu(\mathbf{r})$ ,  $\varepsilon(\mathbf{r})$ ,  $\rho(\mathbf{r})$  and  $K(\mathbf{r})$  are the permeability, permittivity, mass density and bulk modulus at location  $\mathbf{r}$ , respectively. I is a three-component unit tensor and  $\delta(\mathbf{r}-\mathbf{r}')$  is the Dirac's delta source at  $\mathbf{r}'$ . For simplicity, we write the above equations as ZG=I, where Z combines the differential operators and material parameters, and G is Green's function.

The local density of states (LDOS) describes the spatial distribution of the intensity of a single-particle eigenstate, and can be calculated

from the imaginary part of G (in equations (1a) and (1b)) by imposing an infinitesimal imaginary frequency  $\eta$  (refs. 43–45):

LDOS 
$$(\mathbf{r}; \omega) = \frac{2\omega}{\pi} \text{Im} \left\{ \text{Tr} \left[ \varepsilon(\mathbf{r}) \lim_{\eta \to 0^+} G(\mathbf{r}, \mathbf{r}; \omega + i\eta) \right] \right\}$$
 (2a)

LDOS 
$$(\mathbf{r}; \omega) = \frac{2\omega}{\pi} \text{Im} \left[ K^{-1}(\mathbf{r}) \lim_{\eta \to 0^{-}} G(\mathbf{r}, \mathbf{r}; \omega + i\eta) \right]$$
 (2b)

Here, equations (2a) and (2b) are the computational expressions for photonic and acoustic systems, respectively. Tr in equation (2a) signifies tracing Green's tensor, as it is necessary to consider all polarization degrees of freedom in a photonic system.

Because this work mainly focuses on the topological states localized at system boundaries, in the following calculations and analyses we define the surface density of states (SDOS) as the average of the LDOS over the surface layer, unless indicated otherwise.

# **Mathematical origin**

Mathematically, our goal is to efficiently find the corner block inverse of operator Z in equations (1a) and (1b), and to obtain the SDOS using equations (2a) and (2b). When the system exhibits semi-infinite crystal periodicity (as shown in Fig. 1a) and each crystal layer is discretized identically in the finite-element method<sup>46</sup>, the operator transforms into the following form:

$$Z = \begin{pmatrix} Z_{0,0} & Z_{0,1} \\ Z_{1,0} & Z_{0,0} & Z_{0,1} \\ \vdots & \ddots & \ddots \end{pmatrix}$$
 (3)

which is known as the block-Toeplitz (block-cyclic) tridiagonal matrix<sup>19</sup>. Here, diagonal block  $Z_{m,m}$  is the intra-coupling within the mth layer, and the off-diagonal block  $Z_{m,m+1}/Z_{m+1,m}$  is the inter-coupling between neighboring layers; these can be expressed as  $Z_{0,0}$  and  $Z_{0,1}/Z_{1,0}$ , respectively. All these blocks are functions of momenta, considering the periodicity in the closed direction (along the surface).

The CRM and TMM are powerful algorithms for inverting the structured matrix in equation (3). The CRM is based on iteratively inverting an effective coupling matrix for the surface layer, whereas the TMM relies on the eigenanalysis of the transfer matrix for a pair of neighboring layers. The methods deal only with matrices that are the same size or twice the size of  $Z_{0,0}$ , rather than the entire matrix Z, substantially reducing the computational resources required.

This work aims to demonstrate the applicability of these methods to complex photonic and acoustic structures such as those in Fig. 1a–d, corresponding to equations (3) to (6), as well as their advantages in conveniently investigating novel topological surface states for direct experimental comparisons:

$$Z = \begin{pmatrix} Z_{0,0} & Z_{0,1} & & & \\ Z_{1,0} & Z_{1,1} & Z_{1,2} & & & \\ & Z_{2,1} & Z_{1,1} & Z_{1,2} & & \\ & & \ddots & \ddots & \ddots \end{pmatrix}$$
(4)

$$Z = \begin{pmatrix} \ddots & \ddots & \ddots & & & & \\ & \overline{Z}_{1,2} & \overline{Z}_{1,1} & \overline{Z}_{2,1} & & & & \\ & & \overline{Z}_{1,2} & \overline{Z}_{1,1} & \overline{Z}_{1,0} & & & & \\ & & \overline{Z}_{0,1} & \overline{Z}_{0,0} & Z_{0,1} & & & \\ & & & \overline{Z}_{0,1} & Z_{0,0} & Z_{0,1} & & & \\ & & & & \ddots & \ddots & \ddots \end{pmatrix}$$
(5)

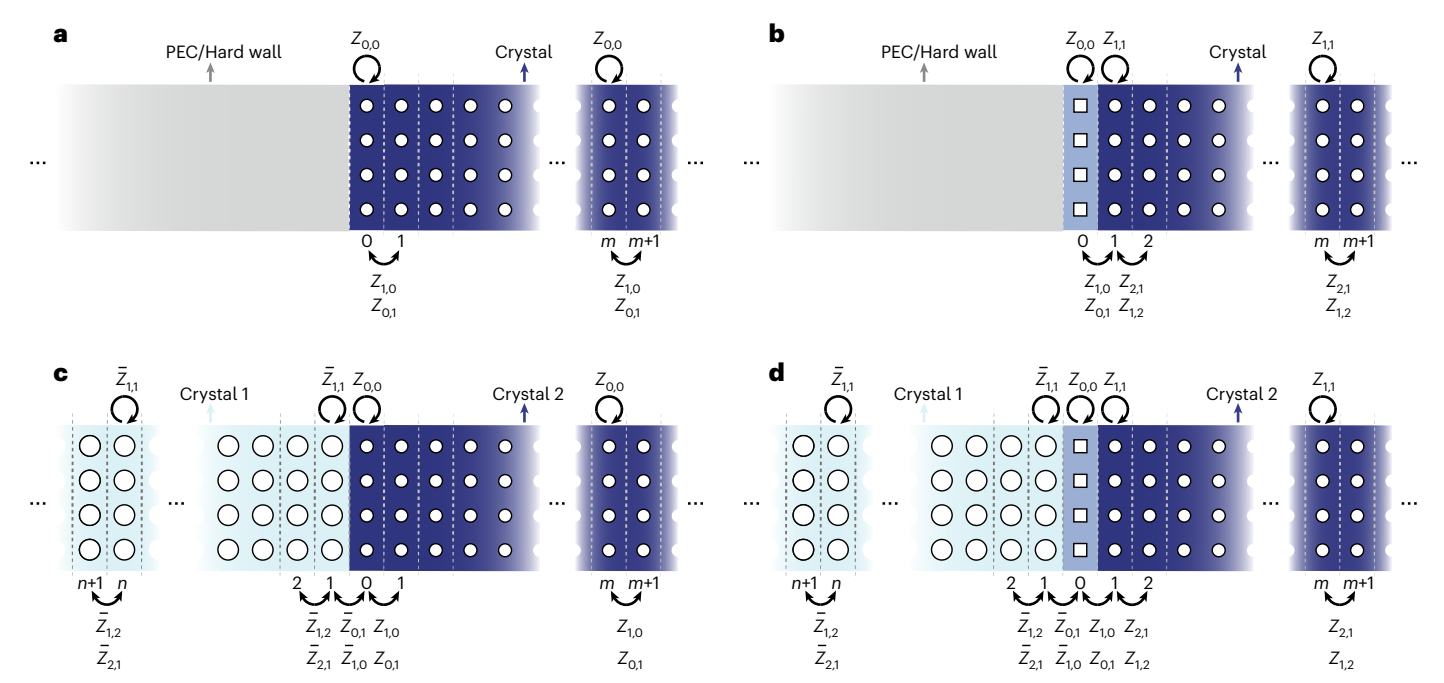


**Fig. 1**| **Various photonic or acoustic crystal structures that support topological surface states.** The structure is divided into layers along the direction perpendicular to the surface indicated by index  $m.Z_{m,m}$  is the intra-coupling matrix within a single layer, and  $Z_{m,m+1}$  and  $Z_{m+1,m}$  are the intercoupling matrices between two nearest-neighbor layers.  $\tilde{Z}$  represents the

coupling matrix in the opposite direction.  $\bf a$ ,  $\bf A$  bare semi-infinite crystal terminated by a perfect electric conductor (PEC)/hard wall.  $\bf b$ ,  $\bf A$  semi-infinite coated crystal terminated by a PEC/hard wall.  $\bf c$ , Two different semi-infinite crystals interfaced with each other.  $\bf d$ , Two different semi-infinite crystals separated by another crystal slab.

$$Z = \begin{pmatrix} \ddots & \ddots & \ddots & & & & & & \\ & \overline{Z}_{1,2} & \overline{Z}_{1,1} & \overline{Z}_{2,1} & & & & & \\ & & \overline{Z}_{1,2} & \overline{Z}_{1,1} & \overline{Z}_{1,0} & & & & \\ & & \overline{Z}_{0,1} & \overline{Z}_{0,0} & \overline{Z}_{0,1} & & & & \\ & & & \overline{Z}_{0,1} & \overline{Z}_{0,0} & \overline{Z}_{0,1} & & & \\ & & & \overline{Z}_{1,0} & \overline{Z}_{1,1} & \overline{Z}_{1,2} & & & \\ & & & \overline{Z}_{2,1} & \overline{Z}_{1,1} & \overline{Z}_{1,2} & & & \\ & & & & \ddots & \ddots & \ddots \end{pmatrix}$$
(6)

# Cyclic reduction method

Here we introduce the CRM in the context of photonics and acoustics. First, let us consider a simple case—a general semi-infinite crystal—as shown in Fig. 1a. To solve for the surface Green's function  $G_{0,0}$ , we now expand equations (1a) and (1b) in a block manner according to equation (3), which gives a series of chain equations:

$$-\zeta_0 G_{m,0} = \alpha_0 G_{m+1,0} + \beta_0 G_{m-1,0}, \ m \ge 1, \tag{7a}$$

$$-\zeta_0^s G_{0,0} = \alpha_0 G_{1,0} - I \tag{7b}$$

where

$$\alpha_0 = Z_{0,1}, \beta_0 = Z_{1,0}, \zeta_0 = Z_{0,0},$$
 (8a)

$$\zeta_0^{\rm s} = Z_{0.0}$$
 (8b)

The superscript *s* here is used to denote surface quantities. Next, we remove the odd-layer Green's functions repeatedly using Gaussian elimination, and equations (7a,7b) and (8a,8b) are transformed into the following forms after *i* iterations:

$$-\zeta_i G_{2^i m, 0} = \alpha_i G_{2^i (m+1), 0} + \beta_i G_{2^i (m-1), 0}, \ m \ge 1, \tag{9a}$$

$$-\zeta_{i}^{s}G_{0,0} = \alpha_{i}G_{2^{i},0} - I \tag{9b}$$

where

$$\alpha_{i} = \alpha_{i-1}(\zeta_{i-1})^{-1}\alpha_{i-1},$$

$$\beta_{i} = \beta_{i-1}(\zeta_{i-1})^{-1}\beta_{i-1},$$

$$\zeta_{i} = \zeta_{i-1} - \alpha_{i-1}(\zeta_{i-1})^{-1}\beta_{i-1} - \beta_{i-1}(\zeta_{i-1})^{-1}\alpha_{i-1},$$
(10a)

$$\zeta_{i}^{s} = \zeta_{i-1}^{s} - \alpha_{i-1}(\zeta_{i-1})^{-1}\beta_{i-1}$$
(10b)

Here, equations (9a,9b) and (10a,10b) define an effective eigenmatrix that builds connections between the layers at intervals of  $2^i$ . As the iterations proceed, the distance between those layers increases exponentially, and the corresponding inter-couplings ( $\alpha_i$  and  $\beta_i$ ) decay exponentially to zero due to the inclusion of a global loss ( $\eta$  in equations (2a,2b)).

Finally, the surface Green's function  $G_{0,0}$  decouples with the bulk one  $G_{2^i,0}$  in equation (9b), and we achieve its approximation:

$$G_{0,0} = \lim_{i \to \infty} \left( \zeta_i^{\mathrm{s}} \right)^{-1} \tag{11}$$

This, in turn, allows for the derivation of the SDOS through equations (2a,2b).

Aside from the bare semi-infinite scenario described above, the CRM can also handle other more complicated situations, such as (line defects between) heterostructures, as shown in Fig. 1b-d. Their associated pseudo-codes are provided in the Supplementary section 1 (Supplementary algorithms 2-4).

### Transfer matrix method

Complementary to the CRM, we can use the TMM to derive the SDOS. This has higher accuracy, but at the cost of computational speed. Here we also choose a bare semi-infinite structure as an example. First, we relate the Green's functions of each layer by introducing a transfer matrix T, which also corresponds to equations (7a,7b):

$$\begin{pmatrix} G_{m+1,0} \\ G_{m,0} \end{pmatrix} = T^m \begin{pmatrix} G_{1,0} \\ G_{0,0} \end{pmatrix}, \ m \ge 1, \tag{12a}$$

$$-Z_{0,0}G_{0,0} = Z_{0,1}G_{1,0} - I (12b)$$

with

$$T = \begin{pmatrix} -Z_{0,1}^{-1} Z_{0,0} & -Z_{0,1}^{-1} Z_{1,0} \\ I & 0 \end{pmatrix}$$
 (13)

Next, we rewrite equation (12a) in the following form:

$$\begin{pmatrix} G_{m+1,0} \\ G_{m,0} \end{pmatrix} = S \Lambda^m \left[ S^{-1} \begin{pmatrix} G_{1,0} \\ G_{0,0} \end{pmatrix} \right]$$
 (14)

where  $\Lambda$  is a diagonal matrix and S is a full matrix consisting of all the eigenvalues and eigenvectors of T, respectively:

$$TS = S\Lambda \tag{15}$$

On analyzing equation (14), it becomes imperative to eliminate the eigenvalues of  $\Lambda$  with moduli greater than 1 to avoid divergence in the Green's functions ( $\Lambda^m = \infty$ ). Consequently, the term enclosed within the square brackets must satisfy the following condition:

$$S^{-1} \begin{pmatrix} G_{1,0} \\ G_{0,0} \end{pmatrix} = \begin{pmatrix} C \\ 0 \end{pmatrix} \tag{16}$$

where C is a constant matrix, 0 is a zero matrix, and their positions correspond to those of eigenvalues with moduli less than 1 and greater than 1 in  $\Lambda$ , respectively. S can then also be arranged as a partition matrix corresponding to the same eigenvalue distribution in  $\Lambda$ :

$$S = \begin{pmatrix} S_2 & S_4 \\ S_1 & S_3 \end{pmatrix} \tag{17}$$

Substituting equation (17) into equation (16), we have a relationship between the surface Green's function  $G_{0,0}$  and the bulk one  $G_{1,0}$ :

$$\begin{pmatrix} G_{1,0} \\ G_{0,0} \end{pmatrix} = S \begin{pmatrix} C \\ 0 \end{pmatrix} = \begin{pmatrix} S_2 C \\ S_1 C \end{pmatrix}$$

$$\Rightarrow G_{1,0} = S_2 S_1^{-1} G_{0,0}$$
(18)

Finally, combining equation (18) with equation (12b), we obtain an explicit expression for the surface Green's function:

$$G_{0,0} = \left(Z_{0,0} + Z_{0,1} S_2 S_1^{-1}\right)^{-1} \tag{19}$$

The SDOS for the semi-infinite system can be accordingly derived via equations (2a) and (2b).

One potential difficulty may arise when the inverse of the inter-coupling matrix  $Z_{0.1}$  in equation (13) does not exist. To

overcome the problem, one can decompose the transfer matrix in the following way:

$$T = T_1^{-1} T_2 = \begin{pmatrix} 0 & I \\ -Z_{0,1} & 0 \end{pmatrix}^{-1} \begin{pmatrix} I & 0 \\ Z_{0,0} & Z_{1,0} \end{pmatrix}$$
 (20)

and transform the standard eigenvalue problem (equation (15)) into a generalized eigenvalue problem to find the eigensolutions of T (ref. 47).

The detailed pseudo-codes for using the TMM to handle other complex structures, as shown in Fig. 1b-d, are summarized in Supplementary section 1 (Supplementary algorithms 6 to 8).

## **Numerical examples**

To showcase the applicability of the CRM and TMM in different complex scenarios, we selected four representative photonic structures (Fig. 2a,d,g,j) for verification, which correspond to the four cases illustrated in Fig. 1a–d. A further three structures are also studied to demonstrate that the developed methodology is equally effective for (1) semi-infinite material/media boundaries (Fig. 3a); (2) acoustic systems (Fig. 3d); and (3) higher-order topological systems (Fig. 3g). For all of these seven examples, we assume continuous translational invariance along the z direction with wavevector component  $k_z = 0$ , and introduce the same imaginary frequency  $\eta = \omega/1,000$  into the original Hermitian systems for proper broadening of the SDOS. Details of these examples are provided in the Methods.

From the results presented in Figs. 2 and 3, it is evident that efficient calculation of the SDOS offers three distinct advantages that complement surface band calculations. First, in the SDOS spectra, the bulk states become genuinely continuous, while the surface states remain discrete, allowing for a clear visualization of the evolution of the surface states, and, in particular, their behaviors within the continuum in frequency—momentum space. Second, the topological states of a single well-defined surface can be obtained directly from the SDOS, mitigating the need to inspect the individual wavefunctions of surface bands to sort out localization on different surfaces. Third, the efficient calculation of SDOS spectra has an experimental advantage: they can be directly compared with observables in near-field scanning experiments in both photonics and acoustics.

### Computing accuracy and efficiency

Both the CRM and TMM can effectively obtain the surface Green's function due to the block-cyclic tridiagonal form of matrix Z in such periodic systems. In the following, we will evaluate and compare the strengths and weaknesses of the CRM and TMM, particularly in terms of computing accuracy and efficiency.

In terms of computational accuracy, the TMM provides higher precision than the CRM. As the TMM directly provides an exact expression for the surface Green's function (equation (19)), its results are more accurate than those of the iterative approach used by the CRM (equation (11)). To illustrate this, we take a one-dimensional (1D) photonic crystal with inversion symmetry <sup>48</sup> as an example to analyze the accuracy and convergence of the CRM, TMM and conventional supercell method (SCM) (Fig. 4). However, it is important to note that the introduction of imaginary frequency  $\eta$  may lead to singularities in the system (such as exceptional points). In this case, T becomes ill-conditioned, which could result in catastrophic round-off error amplification, especially at the edges of the energy bands. One possible approach is to reconstruct the relationship between the Green's functions and LDOS (equations (2a,2b)) at exceptional points<sup>49</sup> so that the aforementioned efficient algorithms can be utilized as usual.

In terms of computational memory, the CRM is more advantageous than the TMM. The TMM's memory consumption primarily comes from the eigenanalysis of matrix T, whereas that of the CRM originates from inverting the self-coupling matrix  $\zeta^s$ . Notably, T has

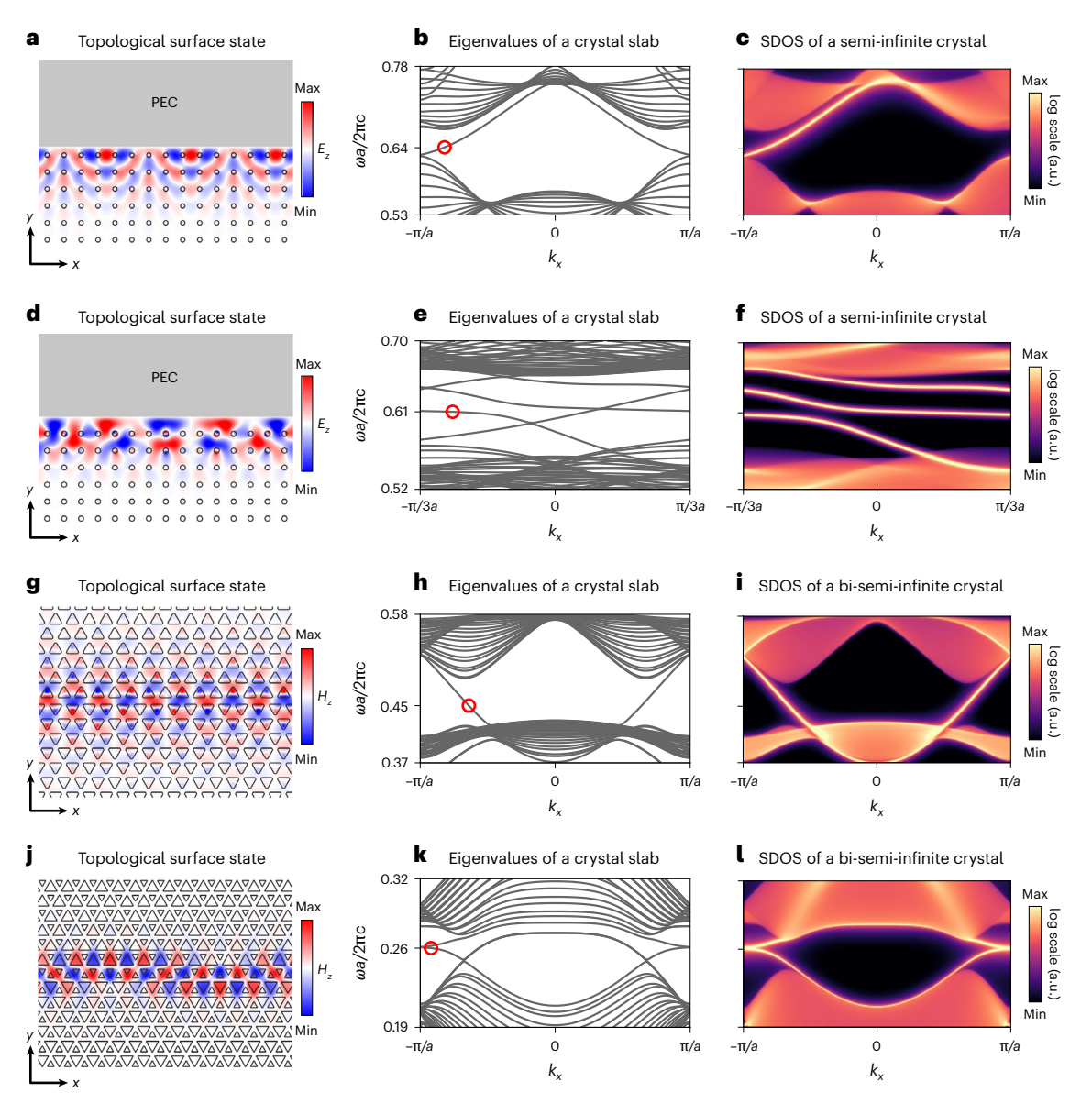


Fig. 2 | Topological surface states of representative surface configurations in photonic crystals. a–I, Topological surface states of a PEC domain wall (a–c), PEC sandwich (d–f), crystal domain wall (g–i) and crystal sandwich (j–I). a, Normalized mode profile  $E_z$  (electric field) of a gyromagnetic photonic crystal terminated by a PEC at a normalized frequency of 0.64c/a, corresponding to the eigenfrequency circled in red in b. b, Band structure of a 12-cell gyromagnetic photonic crystal slab with two PEC boundaries. c, SDOS spectrum of a semi-infinite gyromagnetic photonic crystal with a PEC boundary. d, Normalized mode profile  $E_z$  of a gyromagnetic photonic crystal coated with a crystal slab and terminated by a PEC at a normalized frequency of 0.61c/a, corresponding to the eigenfrequency circled in red in e. e, Band structure of a 13-cell gyromagnetic photonic crystal slab with two PEC boundaries. f, SDOS spectrum of a semi-

infinite gyromagnetic photonic crystal with a PEC boundary.  ${\bf g}$ , Normalized mode profile  $H_z$  (magnetic field) of a valley photonic crystal formed by two semi-infinite crystals face to face at a normalized frequency of 0.45c/a, corresponding to the eigenfrequency circled in red in  ${\bf h}$ .  ${\bf h}$ , Band structure of a 24-cell valley photonic crystal slab with two PEC boundaries.  ${\bf i}$ , SDOS spectrum of a valley photonic crystal extending infinitely on both sides.  ${\bf j}$ , Normalized mode profile  $H_z$  of a valley photonic crystal formed by two semi-infinite crystals separated by another crystal slab at a normalized frequency of 0.26c/a, corresponding to the eigenfrequency circled in red in  ${\bf k}$ .  ${\bf k}$ , Band structure of a 25-cell valley photonic crystal slab with two PEC boundaries.  ${\bf l}$ , SDOS spectrum of a valley photonic crystal extending infinitely on both sides.

twice the degrees of freedom as  $\zeta$  (equations (8b) and (13)), leading to larger memory usage in the TMM. As shown in Table 1, for the same degrees of freedom, the TMM's memory consumption is approximately four times that of the CRM.

In terms of computation time, the CRM is again more advantageous. First, similar to the principle of memory consumption, the time consumption of the TMM primarily stems from the eigenanalysis of matrix T, whereas that of the CRM mainly comes from the inversion of the coupling matrix C. As T has twice the degrees of freedom as C, the time consumption of the TMM is greater. Second, although the time

complexities for both the eigenanalysis and inversion of equivalent matrices are  $O(N^3)$ , the proportionality constant for eigenanalysis is larger, leading to a longer computation time for the TMM. Table 1 also presents the computation time required for both methods, showing that the TMM takes substantially longer than the CRM for the same number of degrees of freedom. It should be noted that the CRM time in Table 1 also has to take into account the number of iterations. Selecting an appropriate imaginary frequency  $\eta$  can effectively reduce the iterations, but at the expense of decreased computational accuracy, as discussed in ref. 40.

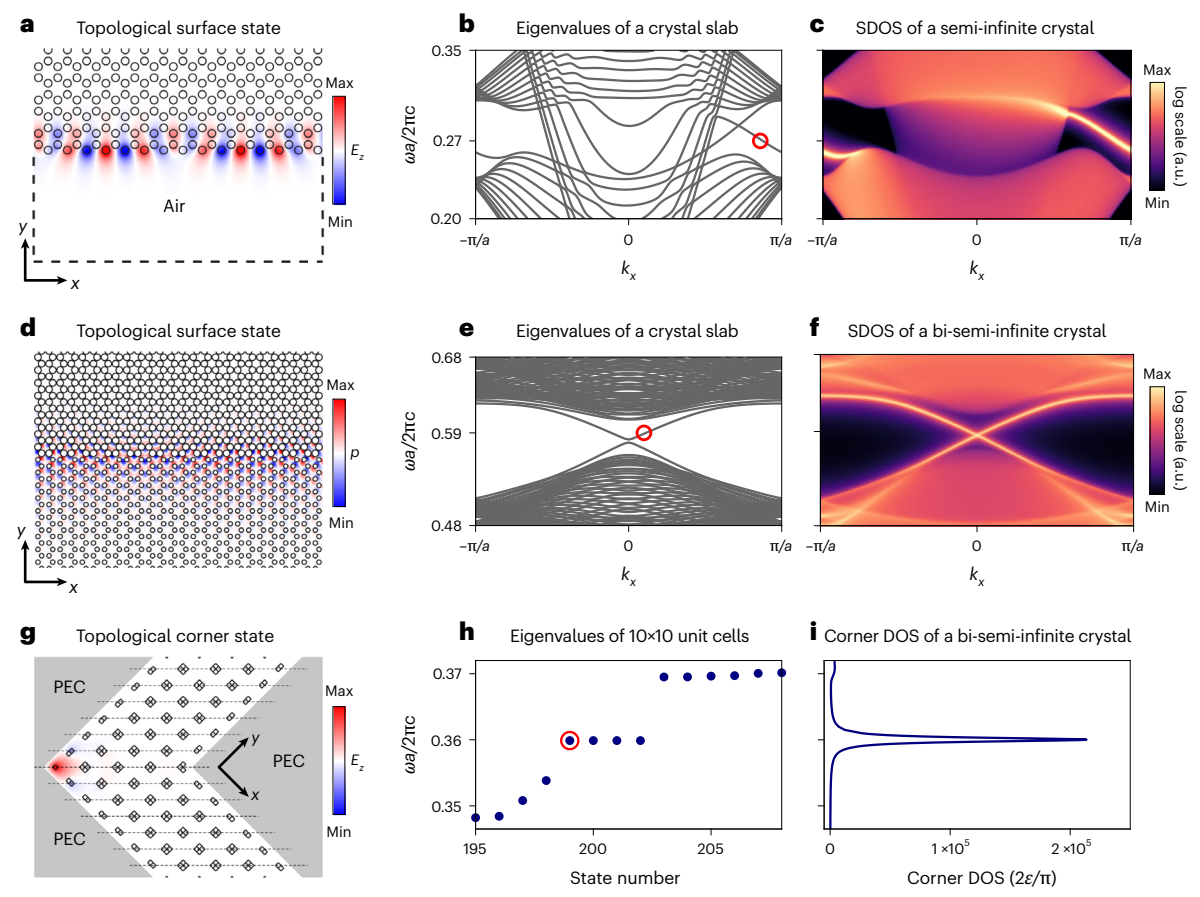


**Fig. 3** | **Topological surface and corner states of three representative configurations. a–i**, Topological surface states of air interface ( $\mathbf{a}$ – $\mathbf{c}$ ), acoustic systems ( $\mathbf{d}$ – $\mathbf{f}$ ) and higher-order topological systems ( $\mathbf{g}$ – $\mathbf{i}$ ). **a**, Normalized mode profile  $E_z$  of a bare semi-infinite gyromagnetic photonic crystal exposed to air at a normalized frequency of 0.27c/a, corresponding to the eigenfrequency circled in red in **b. b**, Band structure of a 12-cell gyromagnetic photonic crystal slab with a PEC and an open boundary. **c**, SDOS spectrum of a gyromagnetic photonic crystal with an open boundary. **d**, Normalized mode profile p (sound pressure) of a spin-Hall acoustic crystal formed by two semi-infinite crystals face to face at a normalized frequency of 0.59c/a, corresponding to the eigenfrequency circled

in red in  ${\bf e}$ .  ${\bf e}$ , Band structure of a spin-Hall acoustic crystal slab with two hard wall boundaries.  ${\bf f}$ , SDOS spectrum of a spin-Hall acoustic crystal extending infinitely on both sides.  ${\bf g}$ , Normalized mode profile  $E_z$  of a quadrupole topological photonic crystal formed by two semi-infinite crystals face to face at a normalized frequency of 0.3599, corresponding to the eigenfrequency circled in red in  ${\bf h}$ .  ${\bf h}$ , Corner eigenvalue spectrum of a finite  $10 \times 10$  photonic crystal enclosed by PEC boundaries with a thin air gap of 0.28a in between.  ${\bf i}$ , Corner density of states spectrum of a quadrupole photonic crystal extending infinitely along primitive vectors  ${\bf a}$  and  ${\bf b}$  but terminated by PECs along the  ${\bf a}$  +  ${\bf b}$  direction.

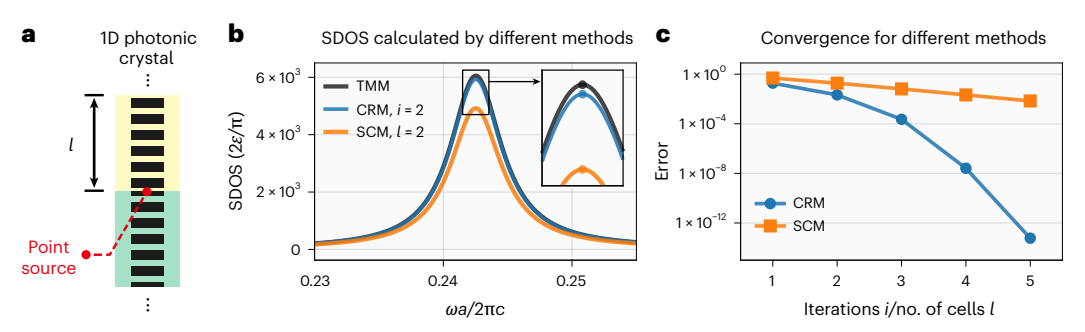


**Fig. 4** | **Accuracy and convergence analyses of the CRM, TMM and SCM. a**, A 1D photonic crystal with inversion symmetry that supports topological interface states. The excitation and receiver are both located at the same point on the interface. **b**, SDOS for a topological state (at the normalized frequency of 0.2425) obtained from different methods. The imaginary frequency is taken as  $\eta = \omega/100$  for finite line broadening. The number of iterations *i* in the CRM and the number of unit cells l (on one side) in the SCM are both set to 2, and the unknown N in

a unit cell is -2,000. It can be observed that the accuracy of the TMM is higher than that of the CRM, and both are superior to the SCM.  $\mathbf{c}$ , Convergence of the different methods. The errors are defined as  $(SDOS_i - SDOS_{i-1})/SDOS_{\infty}$  for the CRM and  $(SDOS_l - SDOS_{i-1})/SDOS_{\infty}$  for the SCM. It can be seen that the error decreases exponentially for the CRM and linearly for the SCM, indicating that the CRM has better convergence.

Table 1 | A comparison of the three methods in terms of memory costs, given by complexities  $O[N^2]$ ,  $O[(2N)^2]$  and  $O[(lN)^2]$ , and time costs, given by complexities  $O[N^3]$ ,  $O[(2N)^3]$ ,  $O[(lN)^3]$ 

Unit cell unknowns (N)	500	1,000	1,500	2,000
Memory for CRM (Mb)	3.82	15.29	34.4	61.16
Memory for TMM (Mb)	15.23	61.04	139.25	244.36
Memory for SCM (Mb)	309.43	1,238.22	2,785.78	4,953.98
Time for CRM (s)	0.006×4	0.036×4	0.11×4	0.26×4
Time for TMM (s)	0.63	5.02	18.27	45.83
Time for SCM (s)	2.34	21.31	69.94	167.71

The performance tests were conducted in MATLAB on an Intel Core i7-12700 CPU (12 cores, 20 threads). The CRM required four iterations, and the SCM utilized nine unit cells, achieving a convergence error of  $1 \times 10^{-4}$  when  $n = \omega/100$ .

It is worth summarizing the respective advantages of the CRM and TMM together with those of the widely used SCM. The CRM is most efficient in terms of time and memory consumption. Meanwhile, although the SCM has slower convergence and thus requires more substantial computational resources, it can directly access the eigenmode profiles (as shown in Figs. 2a,d,g,j and 3a,d,g, calculated with the SCM). Despite the fact that the TMM consumes more time and memory when calculating surface Green's functions than the CRM, it does, however, offers certain other advantages. For example, the intermediate variables (eigenvalues  $\Lambda$  and eigenvectors S) can be used to construct the surface bands (the surface eigenvalues spectrum  $^{50}$ ).

# **Discussions**

In this Article, we have applied two efficient algorithms for calculation of the SDOS in photonic and acoustic crystals, and have investigated the corresponding topological phenomena. The CRM focuses on efficiently solving the SDOS by reducing the computational complexity using Gaussian elimination, whereas the TMM relies on directly solving it through eigenanalysis of a transfer matrix. We have provided numerical examples of various topological photonic and acoustic crystals to demonstrate the utility of these methods.

The key innovation of our work lies in employing finiteelement-type localized basis functions to discretize wavefunctions in continuous optical and acoustic systems, a methodology conceptually analogous to tight-binding theory using localized atomic orbitals for electrons. Compared to traditional plane-wave expansion methods that rely on global basis functions, our approach offers several distinct advantages. First, it enables the precise modeling of arbitrarily complex geometries, such as multiscale structures, through localized mesh refinement, whereas plane-wave methods require prohibitively high expansion orders to achieve comparable accuracy. Second, it effectively handles material systems containing metals or rigid bodies, addressing field discontinuities that challenge the numerical stability of plane-wave expansions. It also naturally accommodates in-plane non-periodic systems, such as finite structures with a PEC or absorbing boundaries, without relying on the reciprocal lattice vectors essential to plane-wave techniques. With geometric flexibility, material versatility and non-periodicity compatibility, our computational framework provides a robust solution for photonic and acoustic systems beyond the constraints of conventional methods. Our method can also be extended to other complex systems, including finite-sized structures, non-uniform interfaces, nonplanar geometries, moiré superlattices and non-Hermitian systems (Supplementary Fig. 1). More detailed information is provided in Supplementary section 2.

The finite-element-based CRM and TMM developed in this work provide substantial improvements over conventional supercell approaches in both computational efficiency and result quality. Computationally, the CRM achieves  $O[N^3]$  complexity by inverting the self-coupling matrix of a single unit cell, whereas the TMM reaches  $O[(2N)^3]$  complexity through eigenvalue analysis of a doubled unit cell. Both methods offer substantial computational savings compared to supercell methods, which scale as  $O[(lN)^3]$  (with  $l \gg 2$  denoting supercell size). Physically, these methods directly handle semi-infinite systems, allowing explicit extraction of surface-specific properties such as SDOS spectra. In contrast, supercell approaches model a finite-sized structure with two surfaces, requiring careful examination of the eigenmodes to exclude states localized at the opposing boundary. Traditional boundary treatments such as perfectly matched layers face challenges because the surface waves are non-radiated and hard to absorb, necessitating specialized techniques such as complex nonlinear coordinate transformations<sup>51</sup> and adiabatic absorbers<sup>52</sup> to address the problems in periodic systems. Furthermore, because our SDOS spectrum retains intensity information, it enables a clear distinction between surface states and bulk continua and facilitates direct tracking of momentum-space evolution for surface states, thereby ensuring quantitative alignment with near-field scanning experimental data.

Our methods may still face challenges in ultra-large-scale simulations, especially for unit cells with millions of degrees of freedom, as in moiré superlattices with small twist angles. In such cases, although our methods can still reduce computational cost, matrix inversion and diagonalization could still consume considerable resources. A useful future direction is parallelization. In our formulation, each SDOS data point is independent in frequency—momentum space, enabling straightforward task decomposition across central processing units or nodes. Moreover, graphics processing unit architectures can also be very well-suited to this problem due to their massive parallelism and high memory bandwidth, which may offer further speed-ups.

# Methods

# **Simulation environment**

All simulations in this study including performance benchmarks and numerical examples, were conducted using COMSOL Multiphysics with a MATLAB scripting interface. It should be noted that the COMSOL in this work is primarily used for mesh generation, which can also be performed by other open-source finite-element meshing tools. The workflow begins by constructing a supercell structure in the COMSOL modeling environment and extracting its finite-sized eigenmatrix Z through MATLAB for traditional SCM validation. This matrix is then partitioned into diagonal self-coupling and off-diagonal inter-coupling submatrices to implement both the CRM and TMM. All performance metrics (computational time, accuracy, memory usage) are thus evaluated under identical model conditions—including consistent geometries and meshing schemes—to ensure rigorous and unbiased comparison of the methods.

# CRM and TMM for coated, hetero- and sandwiched structures

In addition to the methods for bare semi-infinite structures presented in the main text, we extend our analysis to complex configurations. Here we demonstrate this extension through the case of sandwiched structures (Fig. 1d), with the following discussion providing comprehensive methodological details.

In the CRM (Supplementary algorithm 4), we define  $\alpha_0$ ,  $\beta_0$  and  $\overline{\zeta}_0$  as the bulk couplings of a crystal on one side, and  $\bar{\alpha}_0$ ,  $\bar{\beta}_0$  and  $\bar{\zeta}_0$  as the bulk couplings on the other side. We also take  $\alpha_0^s$ ,  $\beta_0^s$ ,  $\bar{\alpha}_0^s$ ,  $\bar{\beta}_0^s$  and  $\zeta_0^s$  as the interface couplings for the sandwiched crystal slab. Here, the overline superscript s denotes quantities in the opposite direction and at the interface, respectively, and subscript t indicates iteration steps. We can then independently iterate the bulk couplings in both directions, and update the interface couplings according to those of the bulk. Finally,

the surface Green's function can be found through  $\zeta_i^s$  if the convergence residual  $(\zeta_i^s - \zeta_{i-1}^s)/(\zeta_{i-1}^s)$  is small enough.

In the TMM (Supplementary algorithm 8), we define  $T_1$ ,  $T_2$  and  $\tilde{T}_1$ ,  $\tilde{T}_2$  as the transfer matrices of crystals on two sides. We can then perform generalized eigenanalyses of the two pairs of transfer matrices independently. By ordering the corresponding eigenvalues and eigenvectors, and combining this with the equation of Green's function at the interface, we can also find the exact solution of the surface Green's function.

### **Details of numerical examples**

The first example is a 2D gyromagnetic photonic crystal with a PEC cladding, which exhibits topological surface states in the second bandgap. Figure 2a presents a schematic of the structure, where the radii of the dielectric pillars are 0.13a, the relative permittivity  $\varepsilon_r$  is 13 and relative permittivity.

the dielectric pillars are 
$$0.13a$$
, the relative permittivity  $\varepsilon_r$  is  $13$  and relative permeability  $\mu_r$  is  $\begin{pmatrix} 1 & -0.4i & 0 \\ 0.4i & 1 & 0 \\ 0 & 0 & 1 \end{pmatrix}$ . We calculate the surface band

structure for a 12-cell crystal slab and the SDOS for a bare semi-infinite crystal, as shown in Fig. 2b,c, respectively. It can be clearly seen that the surface states become more pronounced against the bulk states, and only the chiral state on a single surface is retained in the SDOS spectrum.

Our second example is again a 2D gyromagnetic photonic crystal, but with a surface modification and a PEC cladding, which features topological slow light in the second bandgap. Figure 2d presents a schematic of the structure, where the radii of the dielectric pillars are

$$0.15a$$
, and the relative permeability  $\mu_r$  is  $\begin{pmatrix} 0.83 & -0.42i & 0 \\ 0.42i & 0.83 & 0 \\ 0 & 0 & 1 \end{pmatrix}$ . The relative

permittivity of the surface pillars varies periodically along the x direction in a sequence of  $\varepsilon_r$  = {15, 15, 25}, whereas that of the bulk pillars is uniform at  $\varepsilon_r$  = 15. The surface band structure for a 13-cell crystal slab and the SDOS for a semi-infinite coated crystal are calculated and shown in Fig. 2e,f, respectively. It can be observed that only topological states with negative group velocities are present in the SDOS spectrum, and they exhibit minimal group velocities at the Brillouin zone boundary.

The third example is a 2D valley photonic crystal heterostructure, which supports valley-dependent surface states in the second bandgap  $^{53}$ . Figure 2g provides a schematic of the structure, which is composed of two types of dielectric pillar with opposite orientations. The pillar has a side length of 0.615a and a chamfer length of 0.11a at the corner, with a relative permittivity  $\varepsilon_{\rm r}$  of 13 and permeability  $\mu_{\rm r}$  of 1. We calculate the surface band structure for a 24-cell crystal slab and the SDOS for a heterostructure infinitely extending into both bulks, as shown in Fig. 2h,i, respectively. It becomes apparent that a pair of topological states with opposite group velocities are locked in different valleys in the SDOS spectrum.

The fourth example is again a valley photonic crystal heterostructure, but with a line defect sandwiched at the interface, which supports valley-dependent slow light in the first bandgap  $^{54}$ . Figure 2j shows a schematic of the structure, which consists of three types of dielectric crystal slab. The crystals have a background material relative permittivity  $\varepsilon_{\rm r}$  of 11.56 and permeability  $\mu_{\rm r}$  of 1, with the long and short sides of the air pillars being  $1.3a/\sqrt{3}$  and  $0.7a/\sqrt{3}$ . The surface band structure for a 25-cell crystal slab and the SDOS for a sandwiched structure extending infinitely in both directions are calculated and shown in Fig. 2k,l, respectively. It can be intuitively observed that only the confined modes of the interface exist in the SDOS spectrum, and it shows slow group velocities near the Brillouin zone edge.

The fifth example is a 2D gyromagnetic photonic crystal exposed to air, which has topological surface states in the first bandgap<sup>55</sup>. Figure 3a presents a schematic of the structure, and the radii of the dielectric pillars are 0.2a, with relative permittivity  $\varepsilon_{\rm r}$  of 15.26 and

permeability 
$$\mu_r$$
 of  $\begin{pmatrix} 0.80 & -0.72i & 0 \\ 0.72i & 0.80 & 0 \\ 0 & 0 & 1 \end{pmatrix}$  . We calculate the surface band

structure for a 12-cell crystal slab and the SDOS for a bare semi-infinite crystal interfaced with air, as shown in Fig. 3b,c, respectively. It is noted that only the state of the air-crystal interface remains in the SDOS spectrum. Moreover, information absent in the surface band calculation can be found in the SDOS spectrum—when the topological surface band enters the light cone, it couples to the radiation continuum (in the x-y plane), resulting in their hybridization and blurring of the SDOS of the surface band.

The sixth example is a 2D spin-Hall acoustic crystal, which has pseudospin-dependent topological surface states in the second bandgap<sup>56</sup>. Figure 3d presents a schematic of the structure, and the radii of the rigid bodies on the two sides are 0.3a and 0.45a. We calculate the surface band structure for a 24-cell crystal slab and the SDOS for a structure extending infinitely on both sides, as shown in Fig. 3e,f, respectively. It can be seen from the SDOS spectrum that two pseudospin-locked counterpropagating acoustic modes are equally excited at the same interface.

The last example is a 2D gyromagnetic photonic crystal that supports quadrupole corner states. Figure 3g presents a schematic of the photonic crystal structure, as discussed in ref. 57. The dielectric pillars have a side length of 0.17a, with a relative permittivity  $\varepsilon_r$  of 15 and per-

meability 
$$\mu_r$$
 of  $\begin{pmatrix} 14 & -12.4i & 0 \\ 12.4i & 14 & 0 \\ 0 & 0 & 1 \end{pmatrix}$ . The structure extends infinitely along

the primitive vectors  ${\bf a}$  and  ${\bf b}$  but is terminated by the PEC along the  ${\bf a}+{\bf b}$  direction. By redefining finite-sized supercells along this finite-sized direction as effective unit cells (inside the dashed lines in Fig. 3g), we can apply the algorithms designed for a sandwiched structure to calculate the SDOS and further derive the corner DOS. We calculate the corner eigenvalue spectrum for  $10\times 10$  unit cells and the corner DOS for the bi-semi-infinite structure, which are shown in Fig. 3h,i, respectively. The corner state can be clearly observed within a bandgap in the corner DOS spectrum, which aligns well with the eigenvalue spectrum.

# Data availability

All data in this study were generated by running our codes (ref. 58). Source data are provided with this paper.

# **Code availability**

Source codes associated with this manuscript are available on Zenodo (ref. 58) and via GitHub at https://github.com/YixinSha/SDOS.

# References

- Yuan, L., Lin, Q., Xiao, M. & Fan, S. Synthetic dimension in photonics. Optica 5, 1396–1405 (2018).
- Ozawa, T. et al. Topological photonics. Rev. Mod. Phys. 91, 015006 (2019).
- 3. Ma, S., Yang, B. & Zhang, S. Topological photonics in metamaterials. *Photonics Insights* **1**, R02 (2022).
- 4. Price, H. et al. Roadmap on topological photonics. *J. Phys. Photon.* **4**, 032501 (2022).
- Yang, Z. et al. Topological acoustics. *Phys. Rev. Lett.* **114**, 114301 (2015).
- Ma, G., Xiao, M. & Chan, C. T. Topological phases in acoustic and mechanical systems. *Nat. Rev. Phys.* 1, 281–294 (2019).
- 7. Xue, H., Yang, Y. & Zhang, B. Topological acoustics. *Nat. Rev. Mater.* **7**, 974 (2022).
- 8. Yang, Y. et al. Non-abelian physics in light and sound. *Science* **383**, eadf9621 (2024).
- Chen, M. L. N., Jiang, L., Lan, Z. & Sha, W. E. I. Pseudospinpolarized topological line defects in dielectric photonic crystals. *IEEE Trans. Antennas Propag.* 68, 609–613 (2019).

- Zhang, Z.-D. et al. Topological surface acoustic waves. Phys. Rev. Appl. 16. 044008 (2021).
- Zhang, Z. et al. Directional acoustic antennas based on valley-Hall topological insulators. Adv. Mater. 30, 1803229 (2018).
- Wu, T. et al. Topological photonic lattice for uniform beam splitting, robust routing, and sensitive far-field steering. *Nano Lett.* 23, 3866–3871 (2023).
- Wang, J.-Q. et al. Extended topological valley-locked surface acoustic waves. Nat. Commun. 13, 1324 (2022).
- Bandres, M. A. et al. Topological insulator laser: experiments. Science 359, eaar4005 (2018).
- Zeng, Y. et al. Electrically pumped topological laser with valley edge modes. Nature 578, 246–250 (2020).
- Farmanbar, M., Amlaki, T. & Brocks, G. Green's function approach to edge states in transition metal dichalcogenides. *Phys. Rev. B* 93, 205444 (2016).
- 17. Smidstrup, S. et al. First-principles Green's-function method for surface calculations: a pseudopotential localized basis set approach. *Phys. Rev. B* **96**, 195309 (2017).
- Metalidis, G. & Bruno, P. Green's function technique for studying electron flow in two-dimensional mesoscopic samples. *Phys. Rev.* B 72, 235304 (2005).
- Golub, G. H. & Van Loan, C. F. Matrix Computations (JHU Press, 2013)
- Minchev, B. V. Some algorithms for solving special tridiagonal block Toeplitz linear systems. J. Comput. Appl. Math. 156, 179–200 (2003).
- Velev, J. & Butler, W. On the equivalence of different techniques for evaluating the Green function for a semi-infinite system using a localized basis. J. Phys. Condens. Matter 16, R637 (2004).
- Sancho, M. L., Sancho, J. L., Sancho, J. L. & Rubio, J. Highly convergent schemes for the calculation of bulk and surface Green functions. J. Phys. F 15, 851 (1985).
- Lee, D. & Joannopoulos, J. Simple scheme for surface-band calculations. II. The Green's function. Phys. Rev. B 23, 4997 (1981).
- Golub, G. H. & Varga, R. S. Chebyshev semi-iterative methods, successive overrelaxation iterative methods, and second order Richardson iterative methods. *Numer. Math.* 3, 157–168 (1961).
- Hockney, R. W. A fast direct solution of Poisson's equation using Fourier analysis. J. ACM 12. 95–113 (1965).
- Buzbee, B. L., Golub, G. H. & Nielson, C. W. On direct methods for solving Poisson's equations. SIAM J. Numer. Anal. 7, 627–656 (1970).
- Heller, D. Some aspects of the cyclic reduction algorithm for block tridiagonal linear systems. SIAM J. Numer. Anal. 13, 484 (1976).
- Umerski, A. Closed-form solutions to surface green's functions. Phys. Rev. B 55, 5266 (1997).
- Colbrook, M. J., Roman, B. & Hansen, A. C. How to compute spectra with error control. *Phys. Rev. Lett.* 122, 250201 (2019).
- Colbrook, M. J., Horning, A., Thicke, K. & Watson, A. B. Computing spectral properties of topological insulators without artificial truncation or supercell approximation. *IMA J. Appl. Math.* 88, 1 (2023).
- Nardelli, M. B. Electronic transport in extended systems: application to carbon nanotubes. *Phys. Rev. B* 60, 7828 (1999).
- Rungger, I. & Sanvito, S. Algorithm for the construction of self-energies for electronic transport calculations based on singularity elimination and singular value decomposition. *Phys. Rev. B* 78, 035407 (2008).
- Reuter, M. G., Seideman, T. & Ratner, M. A. Probing the surface-to-bulk transition: a closed-form constant-scaling algorithm for computing subsurface Green functions. *Phys. Rev. B* 83, 085412 (2011).

- Peng, Y., Bao, Y. & von Oppen, F. Boundary Green functions of topological insulators and superconductors. *Phys. Rev. B* 95, 235143 (2017).
- 35. Thicke, K., Watson, A. B. & Lu, J. Computing edge states without hard truncation. SIAM J. Sci. Comput. 43, B323 (2021).
- 36. Lu, J., Marzuola, J. L. & Watson, A. B. Defect resonances of truncated crystal structures. SIAM J. Appl. Math. 82, 49 (2022).
- 37. Schomerus, H. Renormalization approach to the analysis and design of Hermitian and non-Hermitian interfaces. *Phys. Rev. Res.* **5**, 043224 (2023).
- Wu, Q., Zhang, S., Song, H.-F., Troyer, M. & Soluyanov, A. A.
   Wanniertools: an open-source software package for novel topological materials. Comput. Phys. Commun. 224, 405–416 (2018).
- Cheng, H., Sha, Y., Liu, R., Fang, C. & Lu, L. Discovering topological surface states of dirac points. *Phys. Rev. Lett.* 124, 104301 (2020).
- Sha, Y.-X. et al. Surface density of states on semi-infinite topological photonic and acoustic crystals. *Phys. Rev. B* 104, 115131 (2021).
- 41. Li, Z.-Y. & Ho, K.-M. Light propagation in semi-infinite photonic crystals and related waveguide structures. *Phys. Rev. B* **68**, 155101 (2003).
- 42. Che, M. & Li, Z.-Y. Analysis of surface modes in photonic crystals by a plane-wave transfer-matrix method. *J. Opt. Soc. Am. A* **25**, 2177–2184 (2008).
- 43. Novotny, L. & Hecht, B. *Principles of Nano-optics* (Cambridge Univ. Press, 2012)
- 44. Carminati, R. et al. Electromagnetic density of states in complex plasmonic systems. *Surf. Sci. Rep.* **70**, 1–41 (2015).
- Chew, W. C., Sha, W. E. & Dai, Q. Green's dyadic, spectral function, local density of states, and fluctuation dissipation theorem. *Progr. Electromagn. Res.* 166, 147 (2019).
- 46. Jin, J.-M. The Finite Element Method in Electromagnetics (Wiley, 2015)
- Lee, D. & Joannopoulos, J. Renormalization scheme for the transfer-matrix method and the surfaces of wurtzite ZnO. *Phys. Rev. B* 24, 6899 (1981).
- Vaidya, S., Ghorashi, A., Christensen, T., Rechtsman, M. C. & Benalcazar, W. A. Topological phases of photonic crystals under crystalline symmetries. *Phys. Rev. B* 108, 085116 (2023).
- 49. Pick, A. et al. General theory of spontaneous emission near exceptional points. *Opt. Express* **25**, 12325 (2017).
- 50. Lee, D. & Joannopoulos, J. Simple scheme for surface-band calculations. I. *Phys. Rev. B* **23**, 4988 (1981).
- Hugonin, J. P. & Lalanne, P. Perfectly matched layers as nonlinear coordinate transforms: a generalized formalization. J. Opt. Soc. Am. A 22, 1844–1849 (2005).
- Oskooi, A. F., Zhang, L., Avniel, Y. & Johnson, S. G. The failure of perfectly matched layers, and towards their redemption by adiabatic absorbers. Opt. Express 16, 11376–11392 (2008).
- 53. Ma, T. & Shvets, G. All-Si valley–Hall photonic topological insulator. *New J. Phys.* **18**, 025012 (2016).
- 54. Yoshimi, H., Yamaguchi, T., Ota, Y., Arakawa, Y. & Iwamoto, S. Slow light waveguides in topological valley photonic crystals. *Opt. Lett.* **45**, 2648–2651 (2020).
- Poo, Y., Wu, R.-X., Lin, Z., Yang, Y. & Chan, C. T. Experimental realization of self-guiding unidirectional electromagnetic edge states. *Phys. Rev. Lett.* **106**, 093903 (2011).
- 56. He, C. et al. Acoustic topological insulator and robust one-way sound transport. *Nat. Phys.* **12**, 1124–1129 (2016).
- 57. He, L., Addison, Z., Mele, E. J. & Zhen, B. Quadrupole topological photonic crystals. *Nat. Commun.* **11**, 3119 (2020).
- Sha, Y.-X., Xia, M.-Y., Lu, L. & Yang, Y. Surface density of states in topological photonic and acoustic systems. *Zenodo* https://doi.org/10.5281/zenodo.16939967 (2025).

# Acknowledgements

Y.Y. acknowledges support from the National Natural Science Foundation of China Excellent Young Scientists Fund (12222417). the Hong Kong Research Grants Council through the Early Career Scheme (27300924), a Strategic Topics Grant (STG3/E-704/23-N), the Collaborative Research Fund (C7015-24GF), the Areas of Excellence Scheme (AoE/P-604/25-R), the Startup Fund of The University of Hong Kong, Ms. Belinda Hung, the Asian Young Scientist Fellowship, the Croucher Foundation, the New Cornerstone Science Foundation through the Xplorer Prize, and the Alibaba DAMO Academy Young Fellow Award. M.-Y.X. acknowledges support from the National Natural Science Foundation of China (62231001 and 62171005). L.L. acknowledges support from the National Natural Science Foundation of China (12025409), the Chinese Academy of Sciences through the Project for Young Scientists in Basic Research (YSBR-021) and through the IOP-HKUST-Joint Laboratory for Wave Functional Materials Research.

### **Author contributions**

Y.-X.S. and L.L. conceived the idea. Y.-X.S. developed the codes, performed the simulations, and drafted the manuscript. All authors discussed the results and revised the paper. Y.Y. supervised the project.

# **Competing interests**

The authors declare no competing interests.

# **Additional information**

**Supplementary information** The online version contains supplementary material available at https://doi.org/10.1038/s43588-025-00898-3.

Correspondence and requests for materials should be addressed to Yi-Xin Sha or Yi Yang.

**Peer review information** *Nature Computational Science* thanks the anonymous reviewer(s) for their contribution to the peer review of this work. Primary Handling Editor: Jie Pan, in collaboration with the *Nature Computational Science* team.

**Reprints and permissions information** is available at www.nature.com/reprints.

**Publisher's note** Springer Nature remains neutral with regard to jurisdictional claims in published maps and institutional affiliations.

Springer Nature or its licensor (e.g. a society or other partner) holds exclusive rights to this article under a publishing agreement with the author(s) or other rightsholder(s); author self-archiving of the accepted manuscript version of this article is solely governed by the terms of such publishing agreement and applicable law.

© The Author(s), under exclusive licence to Springer Nature America, Inc. 2025